Two-dimensional heterostructures formed by graphenelike ZnO and MgO monolayers for optoelectronic applications

Two dimensional heterostructures formed by graphene-like ZnO and MgO monolayers for optoelectronic applications

Mahsa Seyedmohammadzadeh,[1] Cem Sevik,[2, 3] and Oğuz Gülseren[1, 4, *]

[1]*Department of Physics, Bilkent University, Ankara 06800, Turkey*
[2]*Department of Mechanical Engineering, Faculty of Engineering,*
Eskisehir Technical University, Eskisehir 26555, Turkey.
[3]*Department of Physics & NANOlab Center of Excellence,*
University of Antwerp, Groenenborgerlaan 171, B-2020 Antwerp, Belgium
[4]*TÜBÍTAK Research Institute for Fundamental Sciences, 41470 Gebze, Turkey*
(Dated: October 4, 2022)

Two-dimensional heterostructures are an emerging class of materials for novel applications because of extensive engineering potential by tailoring intriguing properties of different layers as well as the ones arised from their interface. A systematic investigation of mechanical, electronic and optical properties of possible heterostructures formed by bilayer structures graphene-like ZnO and MgO monolayers is presented. Different functionality of each layer makes these heterostructures very appealing for device applications. ZnO layer is convenient for electron transport in these structures, while MgO layer improves electron collection. At the outset, all of the four possible stacking configurations across the heterostructure are mechanically stable. In addition, stability analysis using phonon dispersion reveals that the AB stacking formed by placing the Mg atom on top of the O atom of the ZnO layer is also dynamically stable at zero temperature. Henceforth, we have investigated the optical properties of these stable heterostructures by applying many-body perturbation theory within the framework of GW approximation and solving the Bethe-Salpeter equation. It is demonstrated that strong excitonic effects reduce the optical band gap to the visible light spectrum range. These results show that this new 2D form of ZnO/MgO heterostructures open an avenue for novel optoelectronic device applications.

I. INTRODUCTION

Following the exfoliation of single-layer graphene [1, 2], the theoretical and experimental demonstration of its many outstanding physical properties [3–7] have initiated a new nano-device engineering era. Afterwards, prediction and fabrication of other novel two-dimensional (2D) materials with different functionalities have commenced many investigations. Up to now, several various categories of 2D materials are theoretically predicted or experimentally fabricated. Examples are transitional metal dichalcogenides [8–11], MXenes [12–14], MBenes [15–17] and binary 2D structures of group II-V [18], group III–V [19] and group IV-IV [19]. Besides, 2D materials such as silicene [20, 21], h-BN [2, 22, 23] and phosphorene [24] are already explored. Most recently, Janus monolayers have attracted interest due to their distinguished properties arising from out-of-plane structural asymmetry [25–27].

Among all categories above, van der Waals heterostructures (vdWHs) formed by different monolayers are an emerging class of 2D materials [28, 29] because of enriched functionality of the structure by combining different properties of seperate monolayers. These heterostructures are good candidates for various device applications and are considered a revolutionary class of 2D structures [30] as a consequence of large number of combination possibilities for the heterostructure. Most of the initial studies of vdWHs had focused on structures formed by graphene, h-BN and TMDs. Monolayer graphene on the h-BN substrate is the first fabricated member of this class [31]. Vertical heterostructures of graphene, h-BN and MoS_2 are utilized for fabricating tunnelling diodes and transistors [32, 33]. Enhanced photocurrent generation in layered MoS_2 and WS_2 layers sandwiched between graphene layers have been reported [34, 35]. Besides, light-emitting diodes utilizing quantum wells have been designed and fabricated by combining monolayers of graphene, h-BN and TMDs [36]. Most recently, stacked 2D MoS_2 and bulk Si has been realized for designing infrared photodetector [37].

The fascinating properties of mentioned pionering structures have inspired researchers to probe other novel vdWHs, and several structures have been already explored [38–47]. The most straightforward possible structures within this category are those formed by different binary monolayers. Currently, sustainable energy-related applications of group III-VI [48] and the electronic and optical properties of group III-V [49] vdWHs are studied.

Alongside vdWHs, recent studies have reported 2D layered heterostructures with interlayer bonding [50, 51]. Examples are borophene/graphene [52] and SnP_3/GeP_3 heterostructures [53]. Besides, an *ab initio* study has demonstrated the feasibility of artificial controlling the physical properties of vdWHs by utilizing 2D donor-

* gulseren@fen.bilkent.edu.tr

acceptor heterostructures to create strong bond-like interactions between layers [54]. Interlayer bonding in 2D heterostructures alters the properties of corresponding single layers, which is not so conspicuous in vdWHs [50, 55].

In this article, we presented a systematic investigation of possible heterostructures assembled by binary hexagonal monolayers of ZnO and MgO. Graphene-like ZnO and MgO have been theoretically predicted by density functional theory (DFT) based studies [18, 56]. Theoretical reports for the lattice constant of MgO and ZnO are 3.24 Å and 3.21 Å, respectively. Nonpolar monolayer of ZnO is first observed on Ag(111) [57] and later on Pd(111) [58] and Au(111) [59] surfaces. Moreover, freestanding ZnO multi- and monolayers are presently fabricated [60–63]. Distinct theoretical studies based on GW approximation have estimated a direct bandgap of 3.01 eV [64], 3.18 eV [65] and 4.87 eV [56] for monolayer ZnO, whereas the experimentally measured value are reported as 4.48 eV [66] for monolayer obtained from ZnO(0001)surface and 4 eV [62] for graphene-like ZnO. Furthermore, it is shown that ZnO(0001) surface relaxes to graphene-like ZnO and a bandgap of 4.08 eV is obtained [67] by employing the DFT+U method. The tunability of the electronic and magnetic properties of ZnO is examined by uniaxial strain [68], doping [69–71], noble metal adsorption [72] and chemical functionalization [73]. In the case of MgO, a DFT study using HSE06 functional [74] has predicted an indirect bandgap of 4.69 eV, more an indirect to direct bandgap transition by nitrogen functionalization is reported [75]. Another work using GGA-mBJ [76, 77] functional has reported a direct bandgap of 4.2 eV at Γ point. Besides, the magnetic properties of MgO have been investigated by replacing the O atom with different nonmagnetic dopants [78–80]. It was shown that B and C dopants have magnetic half-metal characteristics, N dopant creates antiferromagnetic behaviour, and F-doped monolayer is a nonmagnetic metal.

In recent years, ZnO-based vdWHs have attracted many researchers, and their applications as photocatalyst for water splitting have been investigated [81–83]. Furthermore, tunable bandgap in WSe_2/ZnO [84], stanene/ZnO [85], ZnO/PtSSe [86], MoSSe/ZnO [87], BP/ZnO [88] and ZnO/ZnX (X = S, Se, Te) [89] are already pointed out. Presently, layered structures of ZnO and MgO have been utilized in various electronic devices. ZnO/MgO dielectrics for metal-insulator-metal capacitor [90], field-effect transistor [91] and Au/MgO/ZnO metal-insulator-semiconductor ultraviolet light emitters are currently fabricated [92]. Using bilayer MgO/ZnO, a smaller leakage current and increased shunt resistance are achieved in organic photovoltaics [92]. MgO raises the short circuit current density and fill factor in such a device. A recent study is demonstrated that microspherical MgO/ZnO bilayer can enhance the stability of

self-powered lead-halide perovskite photodetectors and elevate carrier transport [93]. In particular, a recent experimental study reported that internal piezoelectric polarization fields create robust confined excitions at the 2D interface of nonpolar MgZnO/ZnO heterostructures [94].

Motivated by flourishing properties of MgO/ZnO structures and theoretically predicted close lattice match between graphene-like MgO and ZnO, we have systematically investigated mechanical and optical properties of bilayer vdWHs formed by MgO and ZnO monolayers. A previous study by C. E. Ekuma *et al.* has only presented the electronic and optical properties of MgO/ZnO and MgO/ZnO/MgO heterostructures [95] in one possible stacked structure using HSE06 hybrid functional. However, up to our knowledge, there is not any report for mechanical stabilities of different possible stacking of MgO/ZnO results. In the current study, we investigated the thermodynamical, mechanical and dynamical stabilities of four possible stacking of ZnO/MgO heterostructures. Furthermore, we employed GW approximation for better description of the electronic properties of the mechanically stable heterostructures. Besides, the optical properties are determined by solving the Bethe-Salpeter equation (BSE).

II. COMPUTATIONAL DETAILS

In this work, we considered various stacked heterostructures of MgO/ZnO, which are shown in Fig. 1. In the structure named AA_I, the Mg atom is placed on top of the Zn atoms. In the AA_{II} structure, the O atom, which is in the same plane as the Mg atom, is placed on top of the Zn atom. Basically, this structure can be constructed from the AA_I by rotating the top layer by 60° through the rotation axis through the O–O bond perpendicular to the plane and then shifting it along the armchair direction, Mg moves towards the neighbour O, by a bond length. AB_I structure is formed by shifting the atoms of the upper plane of AA_{II} structure along armchair direction, Mg moves away from the neighbour O towards the center of hexagon of the lower layer, by a bond length. Last structure named AB_{II} is formed by shifting the atoms of the upper plane of AA_I structure along armchair direction, Mg moves towards the neighbour O, by a bond length.

All calculations in this study are carried out using the planewave pseudopotential method [96–99] based on density functional theory (DFT). We employed projector augmented wave-type pseudo potentials for DFT computations within the Perdew–Burke–Ernzerhof (PBE) functional [99, 100], and in order to achieve a better approximation for vdW interactions, we utilized optB86b-vdW functional [101–103]. All computational parameters have been selected after conducting careful convergence tests. For relaxing the structures, a Γ point centered $25 \times 25 \times 1$
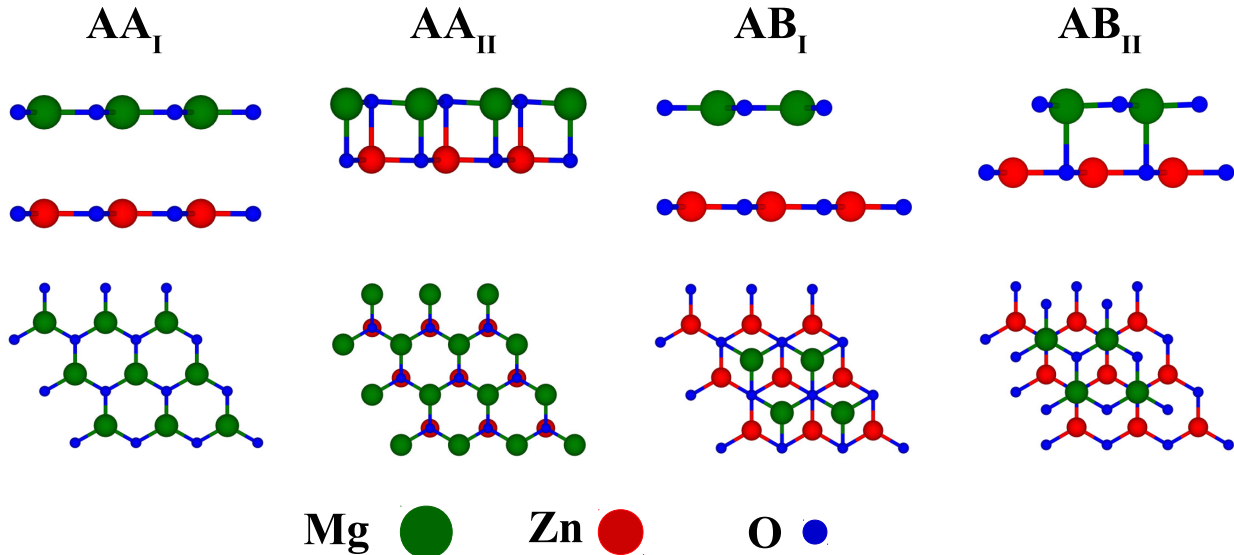
FIG. 1. Top and side views of the possible stacking of ZnO/MgO bilayer heterostructures.

Monkhorst-pack k-point mesh is used for sampling the Brillouin zone (BZ). The kinetic energy cutoff for the plane-wave basis is set to 500 eV. Energy is converged with a tolerance of 10^{-8} eV, and Hellmann–Feynman forces on each atom are minimized to be less than 10^{-3} eV/Å. In order to eliminate the interaction between the layers and their periodic images, a vacuum of 30 Å is introduced between the slabs. Subsequently, a $5 \times 5 \times 1$ supercell and $5 \times 5 \times 1$ k-point mesh are utilized for calculating phonon dispersions. Force constants are calculated using density functional perturbation theory [104], and PHONOPY [105] code is used for calculation of phonon frequencies. In order to include quasiparticle (QP) effects, we performed a single shot of GW calculation (G_0W_0). In the GW approximation, the vertex function in Hedin's equations [106] is neglected, and the self-energy (Σ) is defined as the product of the Green's function (G) and the screened Coulomb potential (W). Using DFT energies ($E_{n\mathbf{k}}$) and orbitals ($\psi_{n\mathbf{k}}$), QP energies ($E_{n\mathbf{k}}^{QP}$) in the G_0W_0 approximation are given by:

$$E_{n\mathbf{k}}^{QP} = E_{n\mathbf{k}} + Z_{n\mathbf{k}} \langle \psi_{n\mathbf{k}} | \Sigma - V_{xc} | \psi_{n\mathbf{k}} \rangle \qquad (1)$$

where the indices $\mathbf{k}$ and n are crystal wave vectors and band numbers, respectively. $Z_{n\mathbf{k}}$ is the renormalization function obtained using the linearization of Σ with a series expansion around the DFT eigenvalues [107]:

$$Z_{n\mathbf{k}} = (1 - \text{Re}(\frac{\partial \Sigma}{\partial \omega}\bigg|_{\omega=E_{n\mathbf{k}}}))^{-1} \qquad (2)$$

In the G_0W_0 calculations, we included 800 bands (26 of them are occupied). While we use 400 eV for the kinetic energy cutoff, the number of frequency grid points is set to 160. The k-point-mesh is generated from $19 \times 19 \times 1$ grid for BZ sampling. All these parameters are selected according to convergence tests (see Fig 5 and discussions in subsection III-B).

QP energies and orbitals are used to construct self-consistent BSE [108, 109] in the Tamm-Dancoff approximation (TDA) [110–112]:

$$\left(E_{c\mathbf{k}}^{QP} - E_{v\mathbf{k}}^{QP}\right) A_{vc\mathbf{k}}^{S} + \sum_{v'c'\mathbf{k}'} \langle vc\mathbf{k} | K_{e-h} | v'c'\mathbf{k}' \rangle A_{v'c'\mathbf{k}'}^{S}$$
$$= \Omega^{S} A_{vc\mathbf{k}}^{S} \qquad (3)$$

here, indices c and v belong to conduction and valence bands, respectively, $A_{vc\mathbf{k}}^{S}$ and Ω^{S} are electron-hole coupling coefficients and corresponding BSE eigenvalues, and K_{e-h} is the kernel for electron-hole interaction. Detailed derivation and explicit form of the matrix elements of K_{e-h} can be found in reference 112 and reference 113. We considered 6 occupied bands and 12 conduction bands for solving the BSE.

III. RESULTS

A. Stability analysis

We first optimized the geometrical structures for the configurations presented in Fig. 1. Lattice parameters of the relaxed structures are given in Table I. The in-plane

lattice constant of AA_I and AB_I structures are almost same, but AA_I has a slightly larger interlayer distance which is in agreement with the previously reported value [95]. The interlayer distance of these configurations is larger than their in-plane lattice constant, i.e. they are comparable with typical van der Waals bond distance. On the other hand, the obtained interlayer distances for AA_{II} and AB_{II} configurations are smaller than their in-plane lattice constants by about 1 Å. In AA_{II} and AB_{II} structures, the Mg atom is placed on top of the O atom of the underlying ZnO layer. The bond length of the Mg–O bond is 2.07 Å and 1.87 Å in its bulk form, rock salt crystal, and in monolayer MgO, respectively [18]. Hence, the calculated interlayer distances of these structures are slightly larger than of the rock salt structure. Therefore, while AA_I and AB_I structures can be considered as vdWHs, AA_{II} and AB_{II} configurations are bonded heterostructures.

We calculated the binding energies of ZnO/MgO heterostructures using the following formula:

$$E_{bind} = E_{tot} - (E_{ZnO} + E_{MgO}) \qquad (4)$$

where E_{tot} is the total energy of the heterostructure, E_{ZnO} and E_{MgO} are the energy of the ZnO and MgO monolayers, respectively. The calculated binding energies are summarized in Table I. Obtained negative binding energies confirm the thermodynamic stability of all structures. The large binding energies of the AA_{II} and AB_{II} structures indicate a strong interaction between the layers.

TABLE I. Calculated in-plane lattice constant (**a**), interlayer distance (**h**), binding energy (**E_bind**) and elastic constants (**C₁₁**) and (**C₁₂**) (both in **Nm⁻¹**) for different stackings.

Configuration	a (Å)	h (Å)	E_bind (meV)	C₁₁	C₁₂
AA_I	3.28	3.76	-92.23	217.62	66.53
AA_{II}	3.36	2.18	-806.49	166.56	49.13
AB_I	3.28	3.53	-113.61	216.76	66.10
AB_{II}	3.32	2.36	-436.53	191.33	59.15

To further study the stability of considered materials, we computed elastic constants using the energy-strain method [114]. In terms of elastic constants C_{ij}, the criteria for mechanical stability of a 2D hexagonal lattice are given by [115, 116]:

$$\begin{aligned} C_{11} &> 0 \\ C_{11} &> |C_{12}| \end{aligned} \qquad (5)$$

The pre-and post-processing steps for calculating elastic constants are carried out using the open-source program VASPKIT [117]. According to obtained results that are presented in Table I all of the configurations are mechanically stable.

To confirm the dynamical stability of the considered systems, we calculated the phonon dispersion curves as presented in Figure 2. Our results show that AB_{II} has no imaginary phonon frequency and is dynamically stable at zero temperature. AA_{II} structure possesses many imaginary frequencies, and its phonon band structure is not presented here (see supplemental material [118]). The AA_{II} structure is dropped from the analysis in the rest of the paper. AA_I and AB_I configurations have imaginary optical phonon frequencies near the center of BZ. These kinds of imaginary frequencies might be cleared by effects like temperature, strain, doping etc. An example of this kind of transition is the surface-functionalized ZnO nanostructures [73, 95]. Other examples are the bulk structures of perovskites that possess imaginary frequencies at the ground state, but temperature-dependent DFT calculations confirmed their dynamical stabilities at room temperatures [119, 120].
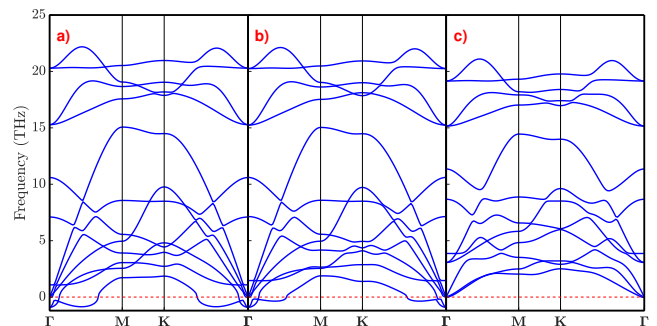

FIG. 2. Calculated phonon dispersion curves for AA_I (a), AB_I (b) and AB_{II} (c).

Apart from the stability of AB_{II}, using the obtained phonon frequencies, it is possible to compare its thermal conductivity (TC) with the monolayer ZnO approximately. A first-principle study within the framework of Boltzmann transport theory has reported a very low TC as 4.5 $Wm^{-1}K^{-1}$ for monolayer ZnO at room temperature [121]. TC of the MgO is obtained as 64 $Wm^{-1}K^{-1}$ utilizing the same procedure [122]. Here we use the Slack equation [123–125] to estimate the thermal conductivity of the AB_{II} configuration. According to the Slack equation, the thermal conductivity can be approximated by the following expression:

$$\kappa = B \frac{\bar{M}\Theta_D^3 \delta n^{\frac{1}{3}}}{\gamma^2 T} \qquad (6)$$

where B is a physical constant, $\bar{M}$ is the average mass of the atoms inside the primitive cell, Θ_D is the Debye temperature, δ^3 is the volume per atom, n is the number of the atoms inside the unit cell, T is the temperature, and γ is the high temperature limit of the Grüneisen

parameter of acoustic modes. Using $\bar{M}$ in atomic mass units and δ in Å, the constant B must be set to 3.6×10^{-6} to get κ in $\text{Wm}^{-1}\text{K}^{-1}$. The Debye temperature can be approximated by following expression:

$$\frac{1}{\Theta_D^3} = \frac{1}{2}\left(\frac{1}{\Theta_{TA}^3 + \Theta_{LA}^3}\right) \qquad (7)$$

The variable $\Theta_i(i = \text{TA}, \text{LA})$, which is defined for the transverse (TA) and longitudinal (LA) acoustic modes, is given by:

$$\Theta_i = \frac{\hbar\omega_{i,max}}{k_B} \qquad (8)$$

where $\hbar$ is the reduced Planck constant, k_B is the Boltzmann constant, and $\omega_{i,max}$ shows the maximum angular frequency of the LA or TA mode. The Grüneisen parameter can be chosen as 2 for all 2D materials as an approximation [125]. It is shown that this value can give a reasonably good estimation for the TC trend of 2D materials. The Debye temperature has been reported to be 287.5 K for monolayer ZnO. Using the phonon frequencies of the AB_{II} structure, we obtained its Debye temperature as 171.27 K. Following reference 121, here we employed the vdW diameter of the oxygen atom (3.04 Å) for the thickness of the layer. The calculated TC for ZnO and AB_{II} structures are 2.75 $\text{Wm}^{-1}\text{K}^{-1}$ and 11.14 $\text{Wm}^{-1}\text{K}^{-1}$, respectively. Despite the inaccuracy arising from the approximations, this result shows that the AB_{II} structure has a smaller TC than monolayer ZnO and MgO.

B. Electronic properties

Next, we investigated the electronic structure of ZnO/MgO heterostructures. The DFT band structures are shown in Fig. 3, and the bandgap values are summarized in Table II. AA_I and AB_I structures exhibit direct band gaps transition at the Γ point, but AB_{II} has an indirect bandgap. Compared to the ZnO and MgO monolayers, the location of maximum of the valence band (VBM) and the minimum of the conduction band (CBM) of the structures indexed by I and II are the same as the ZnO and MgO monolayers, respectively. The DFT bandgap of the AA_I is 1.58 eV, which is larger than of AB_I structure by a small amount of 0.01 eV. The indirect bandgap of AB_{II} is 1.87 eV. This different characteristic of the band gap is another result of the bonded inter-layer nature of the heterostructure. For this structure, the minimum bandgap for a direct transition which is essential in our BSE calculation is located at the Γ point and has a value of 2.13 eV. The LDA bandgaps for ZnO and MgO have been reported as 1.68 eV and 3.68 eV, respectively [18]. In comparison to the large bandgap of MgO, the band gaps of the considered heterostructures are decreased by 57.07% in the case of AA_I, 57.33% in

AB_I and 49.20% in AB_{II}. The DFT bandgap of the AB_{II} structure is 0.19 eV larger than the ZnO monolayer.
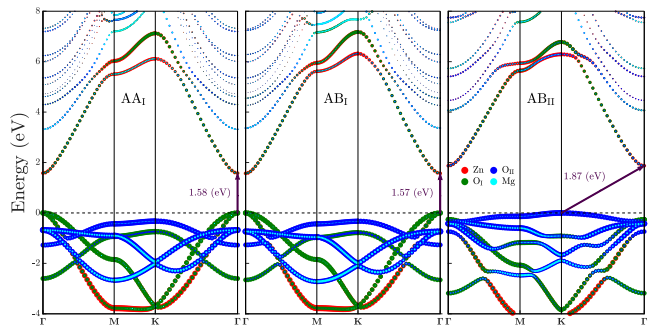

FIG. 3. Electronic band structures of AA_I, AB_I and AB_{II}. The band energies are shifted so that the maximum of the valence band is located at E=0 eV. The arrows show the band gap.

TABLE II. Calculated DFT bandgap (E_{vdW}), G_0W_0 bandgap ($E_{G_0W_0}$), first BSE eigenvalue (E_{BSE}) and exciton binding energies (E_{exc}). All energies are in eV. The direct band gap of the AB_{II} structure (4.42 eV) is used for calculation of the exciton binding energy.

Configuration	E_{vdW}	$E_{G_0W_0}$	E_{BSE}	E_{exc}
AA_I	1.58	3.73	2.50	1.23
AB_I	1.57	3.70	2.49	1.21
AB_{II}	1.87	4.07	3.05	1.37

The contribution of each atom in the band structure is also displayed in Fig. 3. Furthermore, we presented the total density of states (DOS) and orbital decomposed DOS for each atom in mechanically stable structures in Fig. 4. Inspection of Fig. 4 shows that the top of the valence band is dominated by the orbitals from the MgO layer in the AB_{II} structure. In the systems labeled by I, the orbitals of the atoms in the ZnO layer form the top of the valence band. In all structures, Zn atom has the most contribution in the first conduction band. These results show that the MgO layer enriches the electron collection in the bonded bilayer, and the ZnO layer acts as an electron transfer layer.

After this detailed discussion of the band structure, we can identify the band alignment across the heterostructure. The band alignment of these vertical heterostructures, i.e. the bilayer structures formed by different layers A and B, can be determined according to the position of VBM and CBM of the different layers [126]. In straddling (type-I) heterostructures $VBM_A < VBM_B < CBM_B < CBM_A$, hence, electrons and holes are confined in the same region, which can lead to radiative recombinations. Hence, type-I alignment
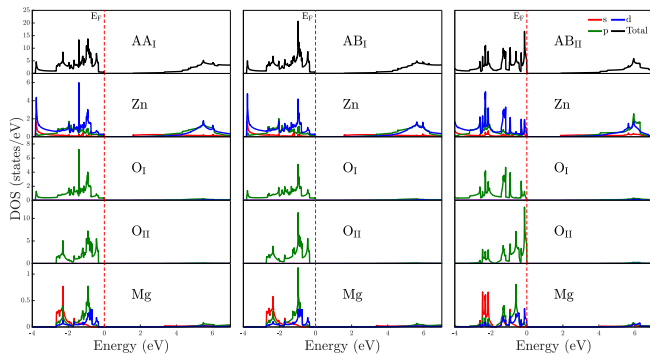
FIG. 4. Total and partial density states of AA_I, AB_I and AB_{II} structures. O_I and O_{II} are the oxygen atoms in the same layer with Zn and Mg atoms, respectively.

is desirable for applications such as light emitting diodes (LEDs). In staggered (type-II) heterostructures, $VBM_A < VBM_B < CBM_A < CBM_B$, therefore VBM and CMB of the type-II heterostructures are placed in different layers that facilitates separation of electrons and holes. Type-II heterostructures are promising for applications such as photovoltaics, photo-detection, solar cells and lasers. In our cases, as we have stated before from band structures, Zn atom has the most contribution in the first conduction band, while the orbitals of the atoms in the ZnO and MgO layers, for structures labeled by I and II respectively, form the top of the valence band. Therefore, AA_I and AB_I heterostructures exhibit type-I band alignment, with $VBM_{MgO} < VBM_{ZnO} < CBM_{ZnO} < CBM_{MgO}$. The band alignment of the AA_I structure is predicted as type-I alignment [95] which is consistent with this result. On the other hand, AB_{II}, $VBM_{ZnO} < VBM_{MgO} < CBM_{ZnO} < CBM_{MgO}$ that indicates type-II band alignment.

We calculated Bader's charges associated with each atom in order to further understand the bonding nature between the atoms. For Bader analysis, the charge attributed to each atom is calculated using the minima of the charge density between the atoms [127–129]. The obtained Bader charges are summarized in Table III. The Bader charges are reported as charge transfer on each atom with respect to their atomic configurations. Therefore, negative charge means electron excess while the positive charge means deficiency. The Bader charges of the structures labeled by I indicate that, approximately, 1.19e is donated by Zn atom to the O atom in the same layer, which received 1.2e in total. The charge transfer is slightly larger in MgO layer, 1.64e of Mg is transfer to O in the same layer, receiving 1.63e in total. Hence, there is only 0.01e transfer from MgO layer to ZnO in these structures, which also verifies their van der Waals character. On the other hand, we observed a more mixed situation in AB_{II} structure. Still,

Zn donates 1.19e and Mg gives away 1.64e similar to the vdWHs, approximately. However, the O of ZnO layer receives 1.24e while the MgO layer O only draws 1.59e. Therefore, the charge transfer from MgO layer to ZnO is slightly larger and increases to 0.04e. This can be interpreted by comparing the bond length of AB_{II} configuration with other structures. According to the lattice constant values summarized in Table I, AB_{II} has a smaller inter-layer separation and metal atoms approach to the inter-layer O atoms. The calculated negative Bader charge for the O_I atom in the AB_{II} structure is 0.043e smaller than the O_I atom in other structures, which shows the interaction between the Mg atom of the AB_{II} structure and the O_I atom, this is consistent with the smaller interlayer distance of the AB_{II} structure. These results show a stronger interaction between the layers in AB_{II} structure consistent with bonded inter-layer nature of the heterostructure.

TABLE III. Calculated Bader charges for each atom in different configurations. O_I and O_{II} are the atoms on ZnO and MgO layers, respectively.

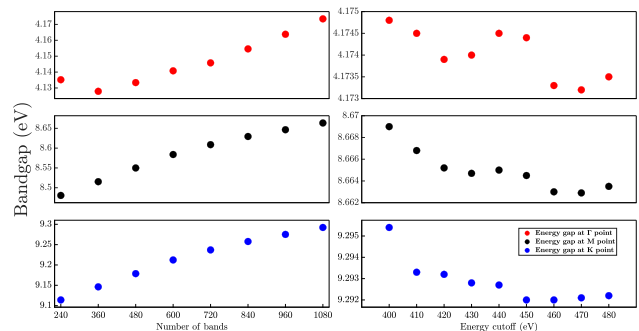| Configuration	Zn	O_I	O_{II}	Mg
AA_I	1.191	-1.199	-1.628	1.636
AB_I	1.187	-1.199	-1.625	1.637
AB_{II}	1.186	-1.242	-1.586	1.642

FIG. 5. Examples of quasiparticle energy convergence tests for AB_I structure with respect to number of bands (left) and energy cutoff (right). For the convergence test of the number of bands, the energy cutoff has been set to 480 eV. For the energy cutoff, 1080 bands are used. In both cases, the number of (imaginary) frequency grid points is chosen as 200, and a vacuum of 30 Å is considered.

Up to now, we have outlined standard electronic properties of the considered structures at the DFT level. At this point, we turn our attention to excited states and excitonic effects for optical properties. First of all, we used G_0W_0 approach for the treatment of the quasiparticle effects. There are several parameters that can affect the accuracy of the GW-BSE method.

First, the number of (imaginary) frequency grid points is chosen as 160 for all cases. Two main factors are the number of unoccupied bands and the energy cutoff for the response function. Furthermore, in the case of the 2D structures, the amount of the vacuum distance considered above the slab is critical because of the long range nature of Columb interaction. The other important factor is the k-point mesh used for BZ sampling. Fully converged results can only be achieved using a very dense k-point mesh [130], i.e. up to $300 \times 300 \times 1$. However, the excessive memory requirements prevent using very dense k-point mesh and a large vacuum distance above the slab. After emphasizing these points, we selected $19 \times 19 \times 1$ k-point mesh and a vacuum of 30 Å for all structures, considering the results of references 131–133. We used $6 \times 6 \times 1$ to estimate the number of the required empty bands and energy cutoff for the response function to minimize the error in the G_0W_0 bandgap up to 0.1 eV. An example of convergence tests is presented in Fig. 5. The G_0W_0 bandgap is very sensitive to the number of empty bands, but the energy cutoff value has a negligible effect on the bandgap of the materials considered in this study. We selected 800 empty bands and an energy cutoff of 400 eV for plane-wave energy, while 2/3 of this value is used for the energy cutoff for the response function. Parameters similar to those selected here were previously used to derive scaling universality between band gap and exciton binding energy of 2D materials [132, 133].

It is commendable to note that utilizing the wave functions from the DFT+U or HSE methods can improve the convergence of the GW calculation for materials with d orbital shells. However, the HSE method imposes a high computational cost, and parameterizing DFT+U is challenging without prior experimental knowledge. In the specific case of the considered 2D materials for assembling the heterostructures considered in this study, it must be pointed out that in the MgO structure, the Mg atom has a full s orbital shell, and correlation effects are not significant in this material. It is evident from the slight difference in the predicted band gap of g-MgO using DFT and HSE [18]. Besides, a good agreement with experimental measurements has been obtained using well converged GW method using KS orbitals [134]. On the other hand, possessing a closed d orbital shell, ZnO must be treated carefully. Determining the structural and electronic properties of bulk ZnO using DFT+U has been considered in several studies. For monolayer ZnO, the band gap from HSE is calculated 50% larger compared to the DFT one [18]. Recently, the effect of Hubbard U correction on the band gap of monolayer ZnO is investigated in detail [135], and it is pointed out that further experimental data is required for the correct selection of the DFT+U parameters. Here, it is worthy to emphasize that GW_0+U_d improves the calculated band gap of bulk ZnO by considering 160 bands for the band summation [136]. Similarly, it is shown that by

increasing the number of unoccupied bands considered in the G_0W_0 calculation, the band gap converges to the experimental value, but $LDA+U+G_0W_0$ converges more rapidly than the $LDA+G_0W_0$ [137]. Furthermore, a similar effect is reported in the case of transition metal oxide perovskites, and the effect of converged number of bands in the results of GW calculations is highlighted [138]. Therefore, although we emphasize the importance of the considered initial orbitals in GW calculations, we rely on DFT orbitals and careful convergence tests performed for selecting the parameters in this study.
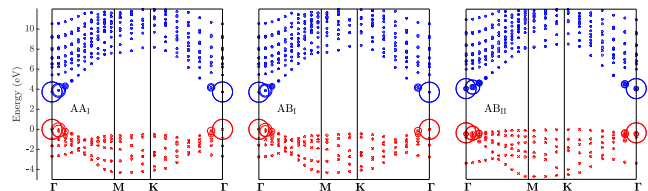

FIG. 6. The band structure calculated by G_0W_0 approach. The circles show the absolute value of the coupling coefficients. The radii of the circles are scaled according to the maximum coupling coefficient and the gap between the band structure.

First, the band structures calculated within G_0W_0 approach are displayed in Fig. 6. Comparison of these with the band structures calculated within the standard DFT approach (see Fig. 3) show that mostly the band gaps increase without much change in band dispersion because of quasiparticle interactions. The obtained bandgaps from G_0W_0 calculations, ($E_{G_0W_0}$), are presented in Table II. The quasiparticle effects increase the bandgaps more than 50%. In all configurations, the calculated $E_{G_0W_0}$ is risen more than twice to the IR region of the spectrum. These relative factors show the similar nature of the electron-hole interaction in different considered systems. As previously pointed out, the results of the GW-BSE method are sensitive to the used computational parameters. Therefore, it is necessary to be careful for an exact quantitative compression between the results obtained in this work and previous literature reports. The G_0W_0 bandgap of monolayer ZnO has been reported to be 4.87 eV [56], 3.18 eV [65], 3.01 eV [64], and 3.98 eV [139]. Compared with the experimentally reported bandgap value of 4.00 eV for graphene-like ZnO [62], the calculated G_0W_0 bandgaps of the AA_I and AB_I are smaller by 0.27 eV 0.3 eV, respectively. AB_{II} possesses a broader bandgap by 0.07 eV.

The first BSE eigenvalues, E_{BSE}, which are used for the calculation of exciton binding energy, (E_{exc}), are also reported in Table II. E_{exc} is just the difference between the first BSE eigenvalue and the corresponding G_0W_0 direct bandgap (see Table II). The first bright exciton of the AB_{II} structure has a binding energy (E_{exc}) of 1.37 eV,

which is the maximum among all configurations. The excitonic eigenstates can be expressed by the sum of eigenstates of the electron-hole pairs:

$$|S\rangle = \sum_{vc\mathbf{k}} A_{vc\mathbf{k}}^S |vc\mathbf{k}\rangle \tag{9}$$

According to equation 9, visualizing coupling coefficients can give information about the electron-hole pairs that contribute more to the specific exciton wave function, denoted by $|S\rangle$. So, the absolute value of BSE coupling coefficients are shown in fatband representation [140] along with the G_0W_0 band structure in Fig. 6. Apparently, the couplings are strong near the Γ point where the direct bandgap is located. In the structures labeled by **I**, only two valence bands from the edge of the valence band (bands number 13 and 12), have large coupling values. In the AB_{II} stacking, notable couplings are also observable for the third valence band from the edge (11'th band).
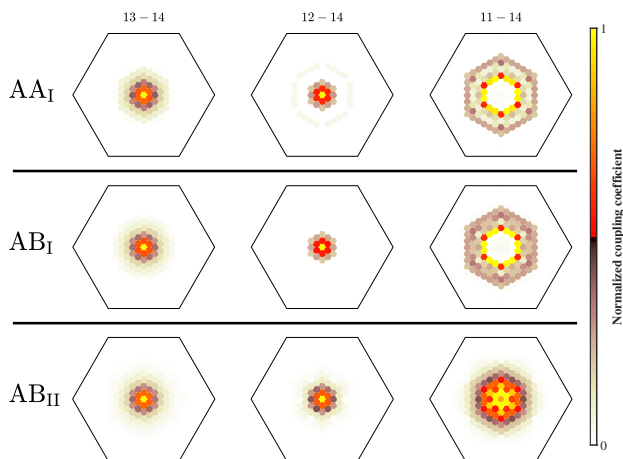

FIG. 7. Distribution of absolute value of electron-hole coupling coefficients for direct transitions from top three valence bands from the edge (bands number 13, 12 and 11) to first conduction band (band number 14). Hexagons show the first Brillouin zone.

In Fig 7, we plotted the absolute values of normalized coupling coefficients between the first conduction band (band number 14) and top three valence bands from the edge in the first BZ. The maximum coupling between the two top valence bands and the first conduction band is located at the Γ point in all structures. The coupling coefficients between the second VB and first CB band vanish more rapidly than those of VBM and CBM (bands 13-14). For AA_I and AB_I, couplings are negligible near the Γ point and edges of the BZ. In AB_{II}, the couplings have considerable values near the Γ point. These behaviours are directly related to the shape of the band structure. For example, in AB_I and AA_I, the minimum distance between the third VB and first CB is located where the maximum coupling coefficient is observed.

C. Optical properties

Next, the optical properties of ZnO/MgO heterostructures will be discussed. The first BSE eigenvalues are listed in Table II. According to these results, the optical band gaps are 2.50 eV, 2.49 eV and 3.05 eV for AA_I and AB_I and AB_{II}, respectively. The imaginary part of the dielectric functions ($Im(\epsilon_x)$ for x-polarized incident light are presented in Fig. 8. The dielectric function of
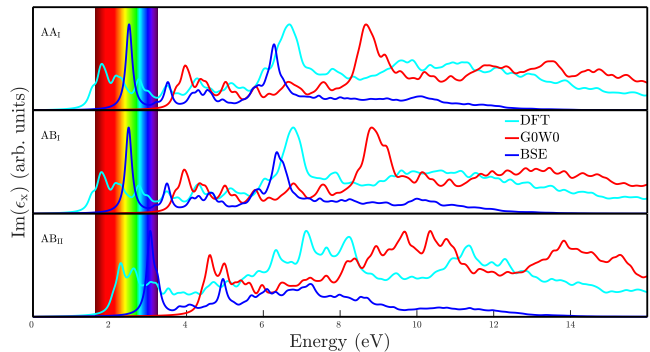

FIG. 8. The imaginary part of the dielectric function for x-polarized incident light for AA_I and AB_I and AB_{II} configurations. Cyan, red and blue curves are the results of the DFT, G_0W_0 and BSE calculations. The visible light spectrum is also shown (from 1.63 eV to 3.26 eV) for reference.

AA_I and AB_I structures, i.e. vdWHs, have very similar shapes. In these two structures, the blue shifts due to quasiparticle effects are reduced by 42.79% and 43.19%. Consequently, the first peaks of the dielectric functions have appeared in the middle of the visible spectrum. Besides, the dielectric functions have a shoulder near the outer edge of the violet light. For x-polarized light, the quasiparticle blue shift in the AB_{II} system is reduced by 46.27%, and the peak of the $Im(\epsilon_x$ is located at the inner edge of the violet light. Similar to other structures, $Im(\epsilon_x$ of AB_{II} also has a shoulder near the first peak, which is located at the outer edge of the violet light spectrum. Calculated optical spectra at the RPA level show that the position of the first peak in the out-of-plane dielectric function of AB_{II} is located (0.48 eV) after the direct band gap (4.42 eV). This distance is much more considerable in AB_I (1.81 eV) and AA_I (1.73 eV). This different behavior might be due to the different nature of the band gap, which is indirect in AB_{II} structure.

In order to gain further insight into excitonic properties, we plotted oscillator strengths along with the imaginary part of the dielectric function corresponding to x-polarized and z-polarized lights as well as the optical absorbance for perpendicular incident light from BSE calculation in Fig. 9. For 2D materials, the amount of incident light that the layer can absorb is quantified by optical absorbance ($A(\omega)$), which can be calculated by
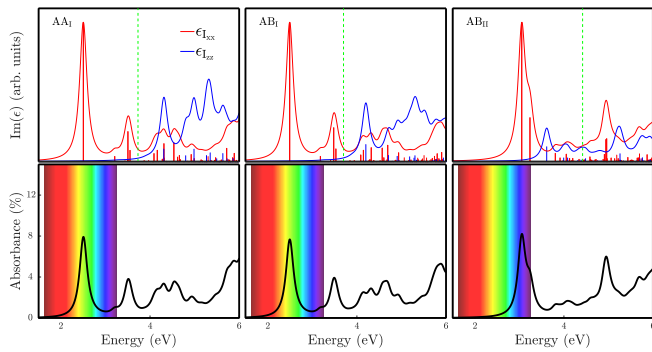
FIG. 9. (Upper row) The imaginary part of the dielectric function for x- and z-polarized incident lights from BSE calculation. Vertical blue and red lines show the oscillator strengths for x- and z-polarized, respectively. Dashed green lines show the position of direct G_0W_0 band gap. (Bottom row) Optical aborbance for perpendicular incident light from BSE calculation.

$A(\omega) = \frac{\omega}{c} L \mathrm{Im}(\epsilon(\omega))$ as described in detail before [141], where c is the speed of light and L is the slab thickness. Despite their small thickness, some 2D materials can absorb considerable incident light. For example, graphene displays an absorbance of 2.3% in the visible light range, equivalent to 20 nm thick Si or 5 nm thick GaAs. Besides, monolayer TMDs such as MoS_2, $MoSe_2$ and WS_2 can absorb up to 5–10% of sunlight. The optical absorbance of the considered structures for the perpendicular incident light is presented in Fig 9. All structures possess a single absorbance peak at the optical band gap, and exhibit optical absorbance values similar to other 2D materials like graphene and TMDs.

The details of optical transitions can be described in terms of oscillator strengths which represent the intensity of the transition for specific excitonic states and are proportional to the sum of the momentum matrix elements [142, 143]. In all of the considered structures,
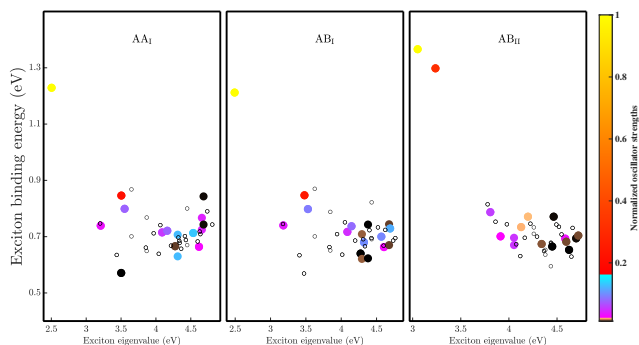

FIG. 10. The exciton binding energies versus exciton eigenvalues for x-polarized incident light. The color bar shows the normalized oscillator strengths and open black circles are used for displaying zero oscillator strengths.

the most considerable oscillator strength appeared at the energy where the first maximum of the $\mathrm{Im}(\epsilon_x)$ is located. As it is expected, the subsequent non-zero oscillator strengths are precisely in accordance with the peaks and shoulders of the dielectric function. In all of the configurations, the first peak of the $\mathrm{Im}(\epsilon_x)$ precedes the first peak of the $\mathrm{Im}(\epsilon_z)$. In the AA_I and AB_I structures, the first peak of the $\mathrm{Im}(\epsilon_z)$ is located after the second peak of $\mathrm{Im}(\epsilon_x)$. In the AB_{II} structure, the first peak of the $\mathrm{Im}(\epsilon_z)$ is located close to the visible light spectrum and appears before the second peak of the $\mathrm{Im}(\epsilon_x)$. By comparing the magnitude of the oscillator strengths, it is also possible to distinguish the dark and bright excitons. The dark excitons are those with zero or negligible oscillator strengths (see Figure 10). Dark excitons with zero oscillator strengths are related to the spin or momentum forbidden transitions [144, 145]. Since the effects of spin polarization and finite momentum are not considered in our approach, the dark excitons in Fig. 10 are related to small transition probabilities. Close energy between the dark and bright excitons can affect the photoluminescence of the nanostructures [146, 147]. Our results show that there is not any dark exciton close to the first BSE eigenvalue of the AA_I and AB_I structures. The first dark exciton of AB_{II} structure appears near the third BSE eigenvalues.

IV. CONCLUSION

In summary, we studied the mechanical, electronic and optical properties of four possible heterostructures formed from ZnO and MgO monolayers. The interlayer distances show that AA_I and AB_I can be considered as vdWH bilayers, however there is an interlayer bonding in AB_{II} and AA_{II} heterostructures. These results are confirmed by comparing the amount of charge transfer between the layers. AA_{II} has many imaginary frequencies in the entire BZ and is dynamically unstable. The AA_I and AB_I have small imaginary phonon frequencies near the center of the BZ. The AB_I structure is dynamically stable at zero temperature. Our band structure calculations based on DFT show that the orbitals of Zn atom dominate the first conduction band of these structures. The MgO layer orbitals dominate the top valence band of the AB_{II} structure. Henceforth, ZnO layer is convenient for electron transport in these structures, while MgO layer improves electron collection. Applying GW-BSE calculations shows strong excitonic effects in MgO/ZnO heterostructures. Our results show that the optical bandgaps of these structures are in the visible light spectrum. These results show that this new 2D form of ZnO/MgO heterostructures open an avenue for novel optoelectronic device applications.

[1] K. S. Novoselov, A. K. Geim, S. V. Morozov, D. Jiang, Y. Zhang, S. V. Dubonos, I. V. Grigorieva, and A. A. Firsov, Electric field effect in atomically thin carbon films, Science **306**, 666 (2004).

[2] K. S. Novoselov, D. Jiang, F. Schedin, T. J. Booth, V. V. Khotkevich, S. V. Morozov, and A. K. Geim, Two-dimensional atomic crystals, Proceedings of the National Academy of Sciences **102**, 10451 (2005).

[3] A. K. Geim and K. S. Novoselov, The rise of graphene, Nature Materials **6**, 183 (2007).

[4] A. H. Castro Neto, F. Guinea, N. M. R. Peres, K. S. Novoselov, and A. K. Geim, The electronic properties of graphene, Rev. Mod. Phys. **81**, 109 (2009).

[5] X. Xu, N. M. Gabor, J. S. Alden, A. M. van der Zande, and P. L. McEuen, Photo-thermoelectric effect at a graphene interface junction, Nano Letters **10**, 562 (2010).

[6] J. H. Seol, I. Jo, A. L. Moore, L. Lindsay, Z. H. Aitken, M. T. Pettes, X. Li, Z. Yao, R. Huang, D. Broido, N. Mingo, R. S. Ruoff, and L. Shi, Two-dimensional phonon transport in supported graphene, Science **328**, 213 (2010).

[7] C. Lee, X. Wei, J. W. Kysar, and J. Hone, Measurement of the elastic properties and intrinsic strength of monolayer graphene, Science **321**, 385 (2008).

[8] B. Radisavljevic, A. Radenovic, J. Brivio, V. Giacometti, and A. Kis, Single-layer mos2 transistors, Nature Nanotechnology **6**, 147 (2011).

[9] J. N. Coleman, M. Lotya, A. O'Neill, S. D. Bergin, P. J. King, U. Khan, K. Young, A. Gaucher, S. De, R. J. Smith, I. V. Shvets, S. K. Arora, G. Stanton, H.-Y. Kim, K. Lee, G. T. Kim, G. S. Duesberg, T. Hallam, J. J. Boland, J. J. Wang, J. F. Donegan, J. C. Grunlan, G. Moriarty, A. Shmeliov, R. J. Nicholls, J. M. Perkins, E. M. Grieveson, K. Theuwissen, D. W. McComb, P. D. Nellist, and V. Nicolosi, Two-dimensional nanosheets produced by liquid exfoliation of layered materials, Science **331**, 568 (2011).

[10] C. Cong, J. Shang, X. Wu, B. Cao, N. Peimyoo, C. Qiu, L. Sun, and T. Yu, Synthesis and optical properties of large-area single-crystalline 2d semiconductor ws2 monolayer from chemical vapor deposition, Advanced Optical Materials **2**, 131 (2014).

[11] K. F. Mak, C. Lee, J. Hone, J. Shan, and T. F. Heinz, Atomically thin mos$_2$: A new direct-gap semiconductor, Phys. Rev. Lett. **105**, 136805 (2010).

[12] M. Naguib, M. Kurtoglu, V. Presser, J. Lu, J. Niu, M. Heon, L. Hultman, Y. Gogotsi, and M. W. Barsoum, Two-dimensional nanocrystals produced by exfoliation of ti3alc2, Advanced Materials **23**, 4248 (2011).

[13] M. Naguib, V. N. Mochalin, M. W. Barsoum, and Y. Gogotsi, 25th anniversary article: Mxenes: A new family of two-dimensional materials, Advanced Materials **26**, 992 (2014).

[14] M. Naguib, J. Halim, J. Lu, K. M. Cook, L. Hultman, Y. Gogotsi, and M. W. Barsoum, New two-dimensional niobium and vanadium carbides as promising materials for li-ion batteries, Journal of the American Chemical Society **135**, 15966 (2013), pMID: 24144164.

[15] L. T. Alameda, P. Moradifar, Z. P. Metzger, N. Alem, and R. E. Schaak, Topochemical deintercalation of al from moalb: Stepwise etching pathway, layered intergrowth structures, and two-dimensional mbene, Journal of the American Chemical Society **140**, 8833 (2018), pMID: 29906120.

[16] X. Yang, C. Shang, S. Zhou, and J. Zhao, Mbenes: emerging 2d materials as efficient electrocatalysts for the nitrogen reduction reaction, Nanoscale Horiz. **5**, 1106 (2020).

[17] Z. Jiang, P. Wang, X. Jiang, and J. Zhao, Mbene (mnb): a new type of 2d metallic ferromagnet with high curie temperature, Nanoscale Horiz. **3**, 335 (2018).

[18] H. Zheng, X.-B. Li, N.-K. Chen, S.-Y. Xie, W. Q. Tian, Y. Chen, H. Xia, S. B. Zhang, and H.-B. Sun, Monolayer ii-vi semiconductors: A first-principles prediction, Phys. Rev. B **92**, 115307 (2015).

[19] H. Şahin, S. Cahangirov, M. Topsakal, E. Bekaroglu, E. Akturk, R. T. Senger, and S. Ciraci, Monolayer honeycomb structures of group-iv elements and iii-v binary compounds: First-principles calculations, Phys. Rev. B **80**, 155453 (2009).

[20] S. Cahangirov, M. Topsakal, E. Aktürk, H. Şahin, and S. Ciraci, Two- and one-dimensional honeycomb structures of silicon and germanium, Phys. Rev. Lett. **102**, 236804 (2009).

[21] P. Vogt, P. De Padova, C. Quaresima, J. Avila, E. Frantzeskakis, M. C. Asensio, A. Resta, B. Ealet, and G. Le Lay, Silicene: Compelling experimental evidence for graphenelike two-dimensional silicon, Phys. Rev. Lett. **108**, 155501 (2012).

[22] F. Paleari, T. Galvani, H. Amara, F. Ducastelle, A. Molina-Sánchez, and L. Wirtz, Excitons in few-layer hexagonal boron nitride: Davydov splitting and surface localization, 2D Materials **5**, 045017 (2018).

[23] C. Elias, P. Valvin, T. Pelini, A. Summerfield, C. J. Mellor, T. S. Cheng, L. Eaves, C. T. Foxon, P. H. Beton, S. V. Novikov, B. Gil, and G. Cassabois, Direct bandgap crossover in epitaxial monolayer boron nitride, Nature Communications **10**, 2639 (2019).

[24] A. H. Woomer, T. W. Farnsworth, J. Hu, R. A. Wells, C. L. Donley, and S. C. Warren, Phosphorene: Synthesis, scale-up, and quantitative optical spectroscopy, ACS Nano **9**, 8869 (2015), pMID: 26256770.

[25] A.-Y. Lu, H. Zhu, J. Xiao, C.-P. Chuu, Y. Han, M.-H. Chiu, C.-C. Cheng, C.-W. Yang, K.-H. Wei, Y. Yang, Y. Wang, D. Sokaras, D. Nordlund, P. Yang, D. A. Muller, M.-Y. Chou, X. Zhang, and L.-J. Li, Janus monolayers of transition metal dichalcogenides, Nature Nanotechnology **12**, 744 (2017).

[26] J. Zhang, S. Jia, I. Kholmanov, L. Dong, D. Er, W. Chen, H. Guo, Z. Jin, V. B. Shenoy, L. Shi, and J. Lou, Janus monolayer transition-metal dichalcogenides, ACS Nano **11**, 8192 (2017), pMID: 28771310.

[27] W. Shi and Z. Wang, Mechanical and electronic properties of janus monolayer transition metal dichalcogenides, Journal of Physics: Condensed Matter **30**, 215301 (2018).

[28] A. K. Geim and I. V. Grigorieva, Van der waals heterostructures, Nature **499**, 419 (2013).

[29] Y. Liu, N. O. Weiss, X. Duan, H.-C. Cheng, Y. Huang, and X. Duan, Van der waals heterostructures and devices, Nature Reviews Materials **1**, 16042 (2016).

[30] X. Wang and F. Xia, Stacked 2d materials shed light, Nature Materials **14**, 264 (2015).

[31] C. R. Dean, A. F. Young, I. Meric, C. Lee, L. Wang, S. Sorgenfrei, K. Watanabe, T. Taniguchi, P. Kim, K. L. Shepard, and J. Hone, Boron nitride substrates for high-quality graphene electronics, Nature Nanotechnology **5**, 722 (2010).

[32] L. Britnell, R. V. Gorbachev, A. K. Geim, L. A. Ponomarenko, A. Mishchenko, M. T. Greenaway, T. M. Fromhold, K. S. Novoselov, and L. Eaves, Resonant tunnelling and negative differential conductance in graphene transistors, Nature Communications **4**, 1794 (2013).

[33] L. Britnell, R. V. Gorbachev, R. Jalil, B. D. Belle, F. Schedin, A. Mishchenko, T. Georgiou, M. I. Katsnelson, L. Eaves, S. V. Morozov, N. M. R. Peres, J. Leist, A. K. Geim, K. S. Novoselov, and L. A. Ponomarenko, Field-effect tunneling transistor based on vertical graphene heterostructures, Science **335**, 947 (2012).

[34] W. J. Yu, Y. Liu, H. Zhou, A. Yin, Z. Li, Y. Huang, and X. Duan, Highly efficient gate-tunable photocurrent generation in vertical heterostructures of layered materials, Nature Nanotechnology **8**, 952 (2013).

[35] L. Britnell, R. M. Ribeiro, A. Eckmann, R. Jalil, B. D. Belle, A. Mishchenko, Y.-J. Kim, R. V. Gorbachev, T. Georgiou, S. V. Morozov, A. N. Grigorenko, A. K. Geim, C. Casiraghi, A. H. C. Neto, and K. S. Novoselov, Strong light-matter interactions in heterostructures of atomically thin films, Science **340**, 1311 (2013).

[36] F. Withers, O. Del Pozo-Zamudio, A. Mishchenko, A. P. Rooney, A. Gholinia, K. Watanabe, T. Taniguchi, S. J. Haigh, A. K. Geim, A. I. Tartakovskii, and K. S. Novoselov, Light-emitting diodes by band-structure engineering in van der waals heterostructures, Nature Materials **14**, 301 (2015).

[37] P. Wu, L. Ye, L. Tong, P. Wang, Y. Wang, H. Wang, H. Ge, Z. Wang, Y. Gu, K. Zhang, Y. Yu, M. Peng, F. Wang, M. Huang, P. Zhou, and W. Hu, Van der waals two-color infrared photodetector, Light: Science & Applications **11**, 6 (2022).

[38] F. Jia, S. Xu, G. Zhao, C. Liu, and W. Ren, Structural and electronic properties of two-dimensional freestanding $BaTiO_3/SrTiO_3$ heterostructures, Phys. Rev. B **101**, 144106 (2020).

[39] K. Rajput and D. R. Roy, Hybrid cas/case bilayer as a wide temperature range thermoelectric material, Physica E: Low-dimensional Systems and Nanostructures **119**, 114014 (2020).

[40] W. Zhang and W. Ji, Two-dimensional van der waals heterostructure cdo/ptse2: promising visible light photocatalyst for overall water splitting, Phys. Chem. Chem. Phys. **22**, 24662 (2020).

[41] H. Li, Y. Xiong, H. Zhang, L. Ye, and W. Li, First-principles study of electric field and strain modulation in gas-bse vdw heterostructured bilayer for bandstructure engineering, Materials Chemistry and Physics **277**, 125615 (2022).

[42] B. Wang, X. Wang, P. Wang, A. Kuang, T. Zhou, H. Yuan, and H. Chen, Bilayer mote2/xs2 (x = hf,sn,zr) heterostructures with efficient carrier separation and light absorption for photocatalytic water splitting into hydrogen, Applied Surface Science **544**, 148842 (2021).

[43] J. Ni, M. Quintana, F. Jia, and S. Song, Tailoring the electronic and optical properties of layered blue phosphorene/ xc (x=ge, si) vdw heterostructures by strain engineering, Physica E: Low-dimensional Systems and Nanostructures **127**, 114460 (2021).

[44] S. Li, M. Sun, J.-P. Chou, J. Wei, H. Xing, and A. Hu, First-principles calculations of the electronic properties of sic-based bilayer and trilayer heterostructures, Phys. Chem. Chem. Phys. **20**, 24726 (2018).

[45] M. Barhoumi, K. Lazaar, and M. Said, Dft study of the electronic and vibrational properties of silicene/stanene heterobilayer, Physica E: Low-dimensional Systems and Nanostructures **111**, 127 (2019).

[46] R. Ahammed, A. Rawat, N. Jena, Dimple, M. K. Mohanta, and A. De Sarkar, Zrs3/ms2 and zrs3/mxy (mmo, w; x, ys, se, te; x neq y) type-ii van der waals hetero-bilayers: Prospective candidates in 2d excitonic solar cells, Applied Surface Science **499**, 143894 (2020).

[47] K. J. Tasnim, S. A. R. Alharbi, M. R. K. Musa, S. H. Lovell, Z. A. Akridge, and M. Yu, Insight into the stacking and the species-ordering dependences of interlayer bonding in SiC/GeC polar heterostructures, Nanotechnology **33**, 155706 (2022).

[48] J. Chen, X. He, B. Sa, J. Zhou, C. Xu, C. Wen, and Z. Sun, Iii–vi van der waals heterostructures for sustainable energy related applications, Nanoscale **11**, 6431 (2019).

[49] X. Lü, S. He, H. Lian, S. Lv, Y. Shen, W. Dong, and Q. Duan, Structural, electronic, and optical properties of pristine and bilayers of hexagonal iii-v binary compounds and their hydrogenated counterparts, Applied Surface Science **531**, 147262 (2020).

[50] Y.-T. Chen, P.-L. Gong, Y.-T. Ren, L. Hu, H. Zhang, J.-L. Wang, L. Huang, and X.-Q. Shi, Interlayer quasi-bonding interactions in 2d layered materials: A classification according to the occupancy of involved energy bands, The Journal of Physical Chemistry Letters **12**, 11998 (2021), pMID: 34890200.

[51] V. Sreepal, M. Yagmurcukardes, K. S. Vasu, D. J. Kelly, S. F. R. Taylor, V. G. Kravets, Z. Kudrynskyi, Z. D. Kovalyuk, A. Patanè, A. N. Grigorenko, S. J. Haigh, C. Hardacre, L. Eaves, H. Sahin, A. K. Geim, F. M. Peeters, and R. R. Nair, Two-dimensional covalent crystals by chemical conversion of thin van der waals materials, Nano Letters **19**, 6475 (2019), pMID: 31426634.

[52] A. Kochaev, K. Katin, M. Maslov, and R. Meftakhutdinov, Aa-stacked borophene-graphene bilayer with covalent bonding: Ab initio investigation of structural, electronic and elastic properties, The Journal of Physical Chemistry Letters **11**, 5668 (2020), pMID: 32586094.

[53] A. Slassi, S. M. Gali, A. Pershin, A. Gali, J. Cornil, and D. Beljonne, Interlayer bonding in two-dimensional ma-

terials: The special case of snp3 and gep3, The Journal of Physical Chemistry Letters **11**, 4503 (2020), pMID: 32419458.

[54] A. H. Woomer, D. L. Druffel, J. D. Sundberg, J. T. Pawlik, and S. C. Warren, Bonding in 2d donor–acceptor heterostructures, Journal of the American Chemical Society **141**, 10300 (2019), pMID: 31189058.

[55] Y. Yin, Y. Hu, S. Li, G. Ding, S. Wang, D. Li, and G. Zhang, Abnormal thermal conductivity enhancement in covalently bonded bilayer borophene allotrope, Nano Research 10.1007/s12274-021-3921-y (2021).

[56] M. Topsakal, S. Cahangirov, E. Bekaroglu, and S. Ciraci, First-principles study of zinc oxide honeycomb structures, Phys. Rev. B **80**, 235119 (2009).

[57] C. Tusche, H. L. Meyerheim, and J. Kirschner, Observation of depolarized zno(0001) monolayers: Formation of unreconstructed planar sheets, Phys. Rev. Lett. **99**, 026102 (2007).

[58] G. Weirum, G. Barcaro, A. Fortunelli, F. Weber, R. Schennach, S. Surnev, and F. P. Netzer, Growth and surface structure of zinc oxide layers on a pd(111) surface, The Journal of Physical Chemistry C **114**, 15432 (2010).

[59] H. Wu, Q. Fu, Y. Li, Y. Cui, R. Wang, N. Su, L. Lin, A. Dong, Y. Ning, F. Yang, and X. Bao, Controlled growth of uniform two-dimensional zno overlayers on au(111) and surface hydroxylation, Nano Research **12**, 2348 (2019).

[60] K. B. Tom, S. Lin, L. F. Wan, J. Wang, N. Ahlm, A. T. N'Diaye, K. Bustillo, J. Huang, Y. Liu, S. Lou, R. Chen, S. Yan, H. Wu, D. Jin, H. Yuan, D. Prendergast, and J. Yao, Solution-based, template-assisted realization of large-scale graphitic zno, ACS Nano **12**, 7554 (2018), pMID: 30011187.

[61] Z. Wang, L. Gan, H. He, and Z. Ye, Free-standing atomically thin zno layers via oxidation of zinc chalcogenide nanosheets, ACS Applied Materials & Interfaces **9**, 13537 (2017), pMID: 28358478.

[62] H.-K. Hong, J. Jo, D. Hwang, J. Lee, N. Y. Kim, S. Son, J. H. Kim, M.-J. Jin, Y. C. Jun, R. Erni, S. K. Kwak, J.-W. Yoo, and Z. Lee, Atomic scale study on growth and heteroepitaxy of zno monolayer on graphene, Nano Letters **17**, 120 (2017), pMID: 28002942.

[63] H. T. Quang, A. Bachmatiuk, A. Dianat, F. Ortmann, J. Zhao, J. H. Warner, J. Eckert, G. Cunniberti, and M. H. Rümmeli, In situ observations of free-standing graphene-like mono- and bilayer zno membranes, ACS Nano **9**, 11408 (2015), pMID: 26446371.

[64] C. Attaccalite, A. Nguer, E. Cannuccia, and M. Grüning, Strong second harmonic generation in sic, zno, gan two-dimensional hexagonal crystals from first-principles many-body calculations, Phys. Chem. Chem. Phys. **17**, 9533 (2015).

[65] W. Wei, Y. Dai, B. Huang, and T. Jacob, Enhanced many-body effects in 2- and 1-dimensional zno structures: A green's function perturbation theory study, The Journal of Chemical Physics **139**, 144703 (2013).

[66] J. Lee, D. C. Sorescu, and X. Deng, Tunable lattice constant and band gap of single- and few-layer zno, The Journal of Physical Chemistry Letters **7**, 1335 (2016), pMID: 27003692.

[67] C. Tan, D. Sun, X. Tian, and Y. Huang, First-principles investigation of phase stability, electronic structure and optical properties of mgzno monolayer, Materials **9**,

[68] B. Rakshit and P. Mahadevan, Indirect to direct bandgap transition under uniaxial strain in layered zno, Applied Physics Letters **102**, 143116 (2013).

[69] L. Chen, A. Wang, Z. Xiong, S. Shi, and Y. Gao, Effect of hole doping and strain modulations on electronic structure and magnetic properties in zno monolayer, Applied Surface Science **467-468**, 22 (2019).

[70] H. Guo, Y. Zhao, N. Lu, E. Kan, X. C. Zeng, X. Wu, and J. Yang, Tunable magnetism in a nonmetal-substituted zno monolayer: A first-principles study, The Journal of Physical Chemistry C **116**, 11336 (2012).

[71] C. Tan, D. Sun, D. Xu, X. Tian, and Y. Huang, Tuning electronic structure and optical properties of zno monolayer by cd doping, Ceramics International **42**, 10997 (2016).

[72] L. Chen, S. Li, Y. Cui, Z. Xiong, H. Luo, and Y. Gao, Manipulating the electronic and magnetic properties of zno monolayer by noble metal adsorption: A first-principles calculations, Applied Surface Science **479**, 440 (2019).

[73] L. Chen, Y. Cui, Z. Xiong, M. Zhou, and Y. Gao, Chemical functionalization of the zno monolayer: structural and electronic properties, RSC Adv. **9**, 21831 (2019).

[74] J. Heyd, G. E. Scuseria, and M. Ernzerhof, Hybrid functionals based on a screened coulomb potential, The Journal of Chemical Physics **118**, 8207 (2003).

[75] D. M. Hoat, V. Van On, D. K. Nguyen, M. Naseri, R. Ponce-Pérez, T. V. Vu, J. F. Rivas-Silva, N. N. Hieu, and G. H. Cocoletzi, Structural, electronic and optical properties of pristine and functionalized mgo monolayers: a first principles study, RSC Adv. **10**, 40411 (2020).

[76] A. D. Becke and E. R. Johnson, A simple effective potential for exchange, The Journal of Chemical Physics **124**, 221101 (2006).

[77] F. Tran and P. Blaha, Accurate band gaps of semiconductors and insulators with a semilocal exchange-correlation potential, Phys. Rev. Lett. **102**, 226401 (2009).

[78] A. D. Moghadam, P. Maskane, and S. Esfandiari, Electronic, magnetic and optical properties of b, c, n and f doped mgo monolayer, Physica C: Superconductivity and its Applications **549**, 33 (2018).

[79] P. Wu, M. Huang, W. Cheng, and F. Tang, First-principles study of b, c, n and f doped graphene-like mgo monolayer, Physica E: Low-dimensional Systems and Nanostructures **81**, 7 (2016).

[80] P. Wu, G. Cao, F. Tang, and M. Huang, Electronic and magnetic properties of transition metal doped mgo sheet: A density-functional study, Computational Materials Science **86**, 180 (2014).

[81] N. Fatima, M. B. Tahir, A. Noor, M. Sagir, M. S. Tahir, H. Alrobei, U. Fatima, K. Shahzad, A. M. Ali, and S. Muhammad, Influence of van der waals heterostructures of 2d materials on catalytic performance of zno and its applications in energy: A review, International Journal of Hydrogen Energy **46**, 25413 (2021).

[82] K. Lazaar, M. Barhoumi, and M. Said, A dft study of gase/aln(zno) two-dimensional vdw heterostructure practiced as an encouraging photocatalyst for water splitting, Computational Materials Science **201**, 110912 (2022).

[83] F. Hu, L. Tao, H. Ye, X. Li, and X. Chen, Zno/wse2 vdw heterostructure for photocatalytic water splitting,

J. Mater. Chem. C **7**, 7104 (2019).

[84] X. Wang, W. Shi, J. Wu, and J. Wan, Anisotropic strain effect on structural and electronic properties in wse2/zno mixed-dimensional heterostructure, Applied Surface Science **551**, 149378 (2021).

[85] H. Cao, Z. Zhou, X. Zhou, and J. Cao, Tunable electronic properties and optical properties of novel stanene/zno heterostructure: First-principles calculation, Computational Materials Science **139**, 179 (2017).

[86] A. Kartamyshev, T. V. Vu, S. Ahmad, S. Al-Qaisi, T. D. Dang, N. L. Tri Dang, and N. N. Hieu, First-principles calculations to investigate electronic properties of zno/ptsse van der waals heterostructure: Effects of vertical strain and electric field, Chemical Physics **551**, 111333 (2021).

[87] Z. Cui, K. Bai, Y. Ding, X. Wang, E. Li, J. Zheng, and S. Wang, Electronic and optical properties of janus mosse and zno vdws heterostructures, Superlattices and Microstructures **140**, 106445 (2020).

[88] R. Zhang, F. Sun, Z. Zhang, J. Liu, Y. Tian, Y. Zhang, X. Wei, T. Guo, J. Fan, L. Ni, and L. Duan, Effective carrier separation in zinc oxide and boron phosphide van der waals heterostructure, Applied Surface Science **535**, 147825 (2021).

[89] C.-M. Lin, C.-F. Chang, W.-C. Hsieh, C.-W. Chang, Y. yuan Zheng, S.-W. Yeh, C.-J. Su, Y.-C. Lin, Y.-H. Yu, C.-W. Chen, C.-C. Kei, C.-H. Liao, K.-S. Huang, K.-T. Huang, D. Chen, W.-K. Chu, L.-W. Tu, P. V. Wadekar, T.-C. Leung, H.-W. Seo, B.-Y. Liaw, and Q. Y. Chen, Electrically tunable bandgaps for g-zno/znx (x = s, se, te) 2d semiconductor bilayers, Vacuum **192**, 110386 (2021).

[90] H. Zulkefle, M. H. Wahid, L. N. Ismail, R. A. Bakar, and M. R. Mahmood, Nanostructures bilayer zno/mgo dielectrics for metal–insulator–metal capacitor applications, Journal of Materials Science: Materials in Electronics **24**, 4213 (2013).

[91] S.-H. Park, W.-P. Hong, and J.-J. Kim, Theoretical studies on the two-dimensional electron-gas properties of mgzno/mgo/zno heterostructures, Journal of the Korean Physical Society **69**, 96 (2016).

[92] C. Zhang, J. Zhang, W. Liu, H. Xu, S. Hou, C. Wang, L. Yang, Z. Wang, X. Wang, and Y. Liu, Enhanced ultraviolet random lasing from au/mgo/zno heterostructure by introducing p-cu2o hole-injection layer, ACS Applied Materials & Interfaces **8**, 31485 (2016), pMID: 27933977.

[93] X. Yang, Y. Zhu, H. Zhou, Z. Song, R. Liu, L. Shen, and H. Wang, Mgo/zno microsphere bilayer structure towards enhancing the stability of the self-powered mapbi3 perovskite photodetectors with high detectivity, Applied Surface Science **504**, 144468 (2020).

[94] M. Zakria, D. J. Rogers, J. Scola, L. Zhu, M. Lockrey, P. Bove, E. V. Sandana, F. H. Teherani, M. R. Phillips, and C. Ton-That, Two-dimensional confinement of excitons at the interface in nonpolar mgzno/zno heterostructures, Phys. Rev. Materials **6**, 035202 (2022).

[95] C. E. Ekuma, S. Najmaei, and M. Dubey, Surface passivated and encapsulated zno atomic layers by high-κ ultrathin mgo layers, Nanoscale **11**, 12502 (2019).

[96] G. Kresse and J. Hafner, Ab initio molecular dynamics for liquid metals, Phys. Rev. B **47**, 558 (1993).

[97] G. Kresse and J. Furthmüller, Efficient iterative schemes for ab initio total-energy calculations using a plane-wave basis set, Phys. Rev. B **54**, 11169 (1996).

[98] G. Kresse and J. Furthmüller, Efficiency of ab-initio total energy calculations for metals and semiconductors using a plane-wave basis set, Computational Materials Science **6**, 15 (1996).

[99] G. Kresse and D. Joubert, From ultrasoft pseudopotentials to the projector augmented-wave method, Phys. Rev. B **59**, 1758 (1999).

[100] P. E. Blöchl, Projector augmented-wave method, Phys. Rev. B **50**, 17953 (1994).

[101] J. Klimeš, D. R. Bowler, and A. Michaelides, Chemical accuracy for the van der waals density functional, Journal of Physics: Condensed Matter **22**, 022201 (2009).

[102] M. Dion, H. Rydberg, E. Schröder, D. C. Langreth, and B. I. Lundqvist, Van der waals density functional for general geometries, Phys. Rev. Lett. **92**, 246401 (2004).

[103] G. Román-Pérez and J. M. Soler, Efficient implementation of a van der waals density functional: Application to double-wall carbon nanotubes, Phys. Rev. Lett. **103**, 096102 (2009).

[104] S. Baroni, S. de Gironcoli, A. Dal Corso, and P. Giannozzi, Phonons and related crystal properties from density-functional perturbation theory, Rev. Mod. Phys. **73**, 515 (2001).

[105] A. Togo and I. Tanaka, First principles phonon calculations in materials science, Scripta Materialia **108**, 1 (2015).

[106] L. Hedin, New method for calculating the one-particle green's function with application to the electron-gas problem, Phys. Rev. **139**, A796 (1965).

[107] M. P. Ljungberg, P. Koval, F. Ferrari, D. Foerster, and D. Sánchez-Portal, Cubic-scaling iterative solution of the bethe-salpeter equation for finite systems, Phys. Rev. B **92**, 075422 (2015).

[108] S. Albrecht, L. Reining, R. Del Sole, and G. Onida, Ab initio calculation of excitonic effects in the optical spectra of semiconductors, Phys. Rev. Lett. **80**, 4510 (1998).

[109] M. Rohlfing and S. G. Louie, Electron-hole excitations in semiconductors and insulators, Phys. Rev. Lett. **81**, 2312 (1998).

[110] S. M. Dancoff, Non-adiabatic meson theory of nuclear forces, Phys. Rev. **78**, 382 (1950).

[111] G. Strinati, Application of the green's functions method to the study of the optical properties of semiconductors, La Rivista del Nuovo Cimento (1978-1999) **11**, 1 (1988).

[112] X. Leng, F. Jin, M. Wei, and Y. Ma, Gw method and bethe–salpeter equation for calculating electronic excitations, WIREs Computational Molecular Science **6**, 532 (2016).

[113] M. Rohlfing and S. G. Louie, Electron-hole excitations and optical spectra from first principles, Phys. Rev. B **62**, 4927 (2000).

[114] Y. Le Page and P. Saxe, Symmetry-general least-squares extraction of elastic coefficients from ab initio total energy calculations, Phys. Rev. B **63**, 174103 (2001).

[115] M. Maździarz, Comment on 'the computational 2d materials database: high-throughput modeling and discovery of atomically thin crystals', 2D Materials **6**, 048001 (2019).

[116] S. Haastrup, M. Strange, M. Pandey, T. Deilmann, P. S. Schmidt, N. F. Hinsche, M. N. Gjerding, D. Torelli, P. M. Larsen, A. C. Riis-Jensen, J. Gath, K. W. Jacobsen, J. J. Mortensen, T. Olsen, and K. S. Thygesen, The

computational 2d materials database: high-throughput modeling and discovery of atomically thin crystals, 2D Materials **5**, 042002 (2018).

[117] V. Wang, N. Xu, J.-C. Liu, G. Tang, and W.-T. Geng, Vaspkit: A user-friendly interface facilitating high-throughput computing and analysis using vasp code, Computer Physics Communications **267**, 108033 (2021).

[118] Note1, See Supplemental Material at [URL will be inserted by publisher] for phonon band structure of AA_{II} structure.

[119] T. Belagodu, E. A. Azhar, and H. Yu, Modulation of charge conduction in zno nanowires through selective surface molecular functionalization, Nanoscale **4**, 7330 (2012).

[120] I. Maeng, S. Lee, H. Tanaka, J.-H. Yun, S. Wang, M. Nakamura, Y.-K. Kwon, and M.-C. Jung, Unique phonon modes of a ch3nh3pbbr3 hybrid perovskite film without the influence of defect structures: an attempt toward a novel thz-based application, NPG Asia Materials **12**, 53 (2020).

[121] H. Wang, G. Qin, G. Li, Q. Wang, and M. Hu, Low thermal conductivity of monolayer zno and its anomalous temperature dependence, Phys. Chem. Chem. Phys. **19**, 12882 (2017).

[122] B. Mortazavi, F. Shojaei, T. Rabczuk, and X. Zhuang, High tensile strength and thermal conductivity in beo monolayer: A first-principles study, FlatChem **28**, 100257 (2021).

[123] G. Slack, Nonmetallic crystals with high thermal conductivity, Journal of Physics and Chemistry of Solids **34**, 321 (1973).

[124] G. A. Slack, The thermal conductivity of nonmetallic crystals (Academic Press, 1979) pp. 1–71.

[125] X. Gu, Y. Wei, X. Yin, B. Li, and R. Yang, Colloquium: Phononic thermal properties of two-dimensional materials, Rev. Mod. Phys. **90**, 041002 (2018).

[126] V. O. Özçelik, J. G. Azadani, C. Yang, S. J. Koester, and T. Low, Band alignment of two-dimensional semiconductors for designing heterostructures with momentum space matching, Phys. Rev. B **94**, 035125 (2016).

[127] E. Sanville, S. D. Kenny, R. Smith, and G. Henkelman, Improved grid-based algorithm for bader charge allocation, Journal of Computational Chemistry **28**, 899 (2007).

[128] G. Henkelman, A. Arnaldsson, and H. Jónsson, A fast and robust algorithm for bader decomposition of charge density, Computational Materials Science **36**, 354 (2006).

[129] W. Tang, E. Sanville, and G. Henkelman, A grid-based bader analysis algorithm without lattice bias, Journal of Physics: Condensed Matter **21**, 084204 (2009).

[130] D. Y. Qiu, F. H. da Jornada, and S. G. Louie, Screening and many-body effects in two-dimensional crystals: Monolayer mos₂, Phys. Rev. B **93**, 235435 (2016).

[131] F. Hüser, T. Olsen, and K. S. Thygesen, How dielectric screening in two-dimensional crystals affects the convergence of excited-state calculations: Monolayer mos₂, Phys. Rev. B **88**, 245309 (2013).

[132] J.-H. Choi, P. Cui, H. Lan, and Z. Zhang, Linear scaling of the exciton binding energy versus the band gap of two-dimensional materials, Phys. Rev. Lett. **115**, 066403 (2015).

[133] Z. Jiang, Z. Liu, Y. Li, and W. Duan, Scaling universality between band gap and exciton binding energy of two-dimensional semiconductors, Phys. Rev. Lett. **118**, 266401 (2017).

[134] W. Gao, W. Xia, X. Gao, and P. Zhang, Speeding up gw calculations to meet the challenge of large scale quasiparticle predictions, Scientific Reports **6**, 36849 (2016).

[135] A. Shokri, A. Yazdani, and K. Rahimi, Possible bandgap values of graphene-like zno in density functional theory corrected by the hubbard u term and hse hybrid functional, Materials Today Communications **22**, 100756 (2020).

[136] Y. Kang, G. Kang, H.-H. Nahm, S.-H. Cho, Y. S. Park, and S. Han, *gw* calculations on post-transition-metal oxides, Phys. Rev. B **89**, 165130 (2014).

[137] B.-C. Shih, Y. Xue, P. Zhang, M. L. Cohen, and S. G. Louie, Quasiparticle band gap of zno: High accuracy from the conventional G^0W^0 approach, Phys. Rev. Lett. **105**, 146401 (2010).

[138] Z. Ergönenc, B. Kim, P. Liu, G. Kresse, and C. Franchini, Converged *gw* quasiparticle energies for transition metal oxide perovskites, Phys. Rev. Materials **2**, 024601 (2018).

[139] Q. Gao, Y. Peng, T. Wang, C. Shen, C. Xia, J. Yang, and Z. Wei, Quantum confinement effects on excitonic properties in the 2d vdw quantum system: The zno/wse2 case, Advanced Photonics Research **2**, 2000114 (2021).

[140] M. Bokdam, T. Sander, A. Stroppa, S. Picozzi, D. D. Sarma, C. Franchini, and G. Kresse, Role of polar phonons in the photo excited state of metal halide perovskites, Scientific Reports **6**, 28618 (2016).

[141] L. Matthes, P. Gori, O. Pulci, and F. Bechstedt, Universal infrared absorbance of two-dimensional honeycomb group-iv crystals, Phys. Rev. B **87**, 035438 (2013).

[142] F. Fuchs, C. Rödl, A. Schleife, and F. Bechstedt, Efficient $\mathcal{O}(N^2)$ approach to solve the bethe-salpeter equation for excitonic bound states, Phys. Rev. B **78**, 085103 (2008).

[143] T. Sander, E. Maggio, and G. Kresse, Beyond the tamm-dancoff approximation for extended systems using exact diagonalization, Phys. Rev. B **92**, 045209 (2015).

[144] T. Mueller and E. Malic, Exciton physics and device application of two-dimensional transition metal dichalcogenide semiconductors, npj 2D Materials and Applications **2**, 29 (2018).

[145] G. Wang, A. Chernikov, M. M. Glazov, T. F. Heinz, X. Marie, T. Amand, and B. Urbaszek, Colloquium: Excitons in atomically thin transition metal dichalcogenides, Rev. Mod. Phys. **90**, 021001 (2018).

[146] T. M. Tumiel, M. Amin, and T. D. Krauss, Single-walled carbon nanotube dark exciton photoluminescence dynamics, The Journal of Physical Chemistry C **125**, 25022 (2021).

[147] H. Yu, M. Laurien, Z. Hu, and O. Rubel, Exploration of the bright and dark exciton landscape and fine structure of mos₂ using g₀w₀-bse, Phys. Rev. B **100**, 125413 (2019).